Supporting Information

Ultrathin Metal Silicate hydroxide Nanosheets with Moderate Metal−Oxygen Covalency Enables Efficient Oxygen Evolution

Jiexin Zhu, Shikun Li, Zechao Zhuang, Shan Gao, Xufeng Hong, Xuelei Pan, Ruohan Yu, Liang Zhou, Lyudmila V. Moskaleva,* Liqiang Mai**

Experimental section

Chemicals. Sodium metasilicate nonahydrate ($Na_2SiO_3 \cdot 9H_2O$, 98%), cobalt chloride hexahydrate ($CoCl_2 \cdot 6H_2O$, Analytical Reagent), iron sulfate heptahydrate ($FeSO_4 \cdot 7H_2O$, Analytical Reagent), nickel chloride hexahydrate ($NiCl_2 \cdot 6H_2O$, Analytical Reagent) and potassium hydroxide (KOH, 99.999%) were purchased from Aladdin Industrial Inc. (Shanghai, China).

Synthesis of CoSHN, FeSHN and NiSHN electrocatalysts. The metal silicate hydroxide nanosheets were prepared by a hydrothermal method. In a typical procedure, $Na_2SiO_3 \cdot 9H_2O$ (2.0 mmol) was dissolved in 40 mL of deionized water and $CoCl_2 \cdot 6H_2O$ (3.0 mmol) was dissolved in 40 mL deionized water under vigorous stirring for 15 min. Then, two solutions were mixed and stirred for 10 min. Afterward, the above mixed solution was transferred into a sealed Teflon-lined stainless-steel autoclave and subsequently heated at 200 °C for 24 h. The obtained cobalt silicate hydroxide powder was washed with deionized water before drying by vacuum freeze-drying. The preparation process of FeSHN and NiSHN was similar to that of CoSHN, except that the $CoCl_2 \cdot 6H_2O$ was replaced by $FeSO_4 \cdot 7H_2O$ and $NiCl_2 \cdot 6H_2O$ for FeSHN or NiSHN, respectively.

Materials characterizations. The as-synthesized products were characterized with a D8 Advance X-ray diffractometer using Cu-Kα radiation (λ = 1.5418 Å). The geometric morphology of the samples was disclosed by transmission electron microscope (TEM, JEOL JEM-2100F/Titan G2 60-300). Energy-dispersive X-ray (EDX) elemental mapping was conducted on an Oxford IE250 (Oxford Instruments, UK) system. Fourier transform infrared (FT-IR) transmittance spectra were recorded using a Nicolet 6700 (Thermo Fisher Scientific Co., USA) IR spectrometer. X-ray photoelectron spectroscopy (XPS) measurements were

performed using a VG MultiLab 2000 instrument. Brunauer-Emmett-Teller (BET) surface areas were measured using a Tristar II 3020 instrument by the adsorption of nitrogen at 77 K. Temperature-dependent magnetic susceptibility (M−T) plots were measured in the temperature range from 50 to 300 K under H = 2 kOe with a magnetic property measurement system model SQUID-VSM (Quantum Design, USA). Electron spin resonance (ESR) spectra were recorded by an ER200-SRC-10/12 (Bruker, Germany) spectrometer at 300 K. O_2 temperature-programmed desorption (O_2-TPD) was measured using TPDRO1100 automatic temperature programmed chemical adsorption instrument. Thickness characterization is performed by atomic force microscope (AFM, AIST, AIST-NT SmartSPM).

X-ray absorption measurements. O K-edge X-ray absorption (XAS) were measured at the beamline BL10B of National Synchrotron Radiation Laboratory (NSRL, Hefei) in the total electron yield mode by collecting the sample drain current under a vacuum better than 10^{-7} Pa. All spectra were normalized to the absorption background at the energy ranges of 520 - 560 eV.

Electrochemical tests. The OER measurements were performed using a conventional three-electrode system using an electrochemical workstation (CHI 760D, Shanghai Chenhua Instrument Co. Ltd.) and modulated speed rotator (MSR, AFMSRCE, rotate speed: 50-10000 rpm, PINE) in a 1.0 M KOH (pH = 13.7) aqueous solution. The glassy-carbon electrode (GCE, diameter = 0.5 cm) with UMSHN ink, platinum plate (Pt, 1 cm × 1 cm), and Hg/HgO (0.098 V vs. a standard hydrogen electrode) were used as the working electrode, counter electrode, and reference electrode, respectively. To make the tests rigorous and avoid iron-based impurities, high-purity KOH (99.999%) was used to prepare the 1.0 M electrolyte in a polytetrafluoroethylene (PTFE) bottle. The potential values were referenced to the reversible

hydrogen electrode (RHE) according to the formula E(RHE) = E(Hg/HgO) + 0.098 + 0.059 × pH and *iR* corrected.

The electrocatalyst inks were prepared using a mixture of 0.2 mL water, 0.75 mL ethanol, 0.05 mL 5 wt% Nafion solution, 5 mg of the UMSHN catalysts, and 5 mg carbon black (Vulcan XC-72R) followed by ultrasonication for 1 h. Then, 10 μL of the ink was uniformly loaded onto a freshly polished glassy-carbon electrode (GCE, diameter = 0.5 cm), which was used as the working electrode yielding a catalyst loading of 0.25 mg cm^{-2}.

Prior to recording the electroactivity of the catalysts, the electrochemical accessibility of the working electrode was optimized by potential cycling between 1.1 and 1.7 V at 100 mV s^{-1} in 1.0 M KOH until stable voltammogram curves were obtained. Then, the cyclic voltammetry (CV) curves were recorded at scan rates of 10 mV s^{-1} and the overpotential (η) at j = 10 mA cm^{-2} was determined using the following equation: $\eta = E$ (*vs.* RHE) − 1.23 V. Tafel plots of the samples were obtained by plotting η against the logarithm of j using the Tafel equation (η = a log j + b, where a is the slope and b is a constant). A long-term stability test was performed at j = 10 mA cm^{-2} for 120 min. The effective electrochemical surface area (ECSA) of electrocatalysts was estimated by performing CV in the potential range of 1.15 to 1.2 V *vs.* RHE at different scan rates (v) of 10, 20, 30, 40, 50, 60, 70, 80, 90 and 100 mV s^{-1}, followed by extracting the slope from the resulting $\Delta j = (j_a - j_c)/2$ *vs.* v plots (j_a and j_c represent the anodic and cathodic current densities normalized to the surface areas of the catalysts at 1.175 V *vs.* RHE). All the electrochemical measurements were conducted at room temperature. Turnover frequency (TOF) values were calculated according to the following equation: TOF = j × A/(4 × F × n), where j is the current density at a given potential, A is the surface of the electrode, n is the mole number of metal atoms on the electrode, and F is Faraday constant. Note that, in the

calculations all metal atoms are assumed to be catalytically active. However, because a fraction of metal sites might not contribute to the catalytic reaction, the calculated TOF represents a lower limit.

Determination of e_g occupancy. The effective magnetic moments (μ_{eff}) for all the samples are obtained by $\mu = \sqrt{8C}\mu_B$, where C is Curie constant and obtained from the fittings of the susceptibility (χ = M/H) above 150 K by a Curie-Weiss law. Using these values, the volume fractions of metal ions in HS and LS states can be calculated from the relationship: $\mu_{eff} = g\mu_B\sqrt{S_{HS}(S_{HS}+1)V_{HS}+S_{LS}(S_{LS}+1)V_{LS}}$, where S_{HS} (= 2) and S_{LS} (= 0) are the S values, and V_{HS} and V_{LS} (= 1 – V_{HS}) are the volume fractions for metal ions in HS and LS states, respectively. Consequently, the e_g electron (χ) can be further calculated by $\chi = S_{HS} \times V_{HS} + S_{LS} \times V_{LS} = 2\ V_{HS}$.

In-situ Raman measurements. Raman spectra was obtained by Horiba LabRAM HR Evolution. The Raman spectra were acquired with He/Ne laser of λ = 633 nm and 4.9 mW. The cyclic voltammetry (CV) curves were performed by an electrochemical workstation (Autolab PGSTAT 204) in a customized Teflon cell with 1 M KOH solution. A glassy carbon electrode worked as the working electrode, an Ag/AgCl electrode as the reference electrode and a polished platinum wire as the counter electrode. The prepare process of electrocatalysts ink is the same as the process described aboved. Then, 10 μL of the ink was uniformly loaded onto a freshly polished glassy-carbon electrode (GCE, diameter = 0.5 cm), which was used as the working electrode yielding a catalyst loading of 0.25 mg cm^{-2}. The potential values were referenced to the RHE without *iR* corrected. To exclude the disturb of produced bubbles, each curve is recorded after adjusting the focal length.

Computational Methods and Models. All of calculations were performed by Vienna ab initio simulation package (VASP)[1, 2] using the Perdew-Burke-Ernzerhof (PBE) functional[3, 4] and the projector augmented wave (PAW)[5, 6] method. Structural optimization, vibrational frequencies, single-point energies and density of states (DOS) calculations were conducted on the same plane-wave cutoff energy, 450 eV, and the same 4 x 4 x 6 Monkhorst-Pack mesh[7] for the integration of Brillouin zone. The optimized geometries and single-point energies converged until the force acting on each atom being less than 0.02 eV/Å and the total energy converging within 10^{-6} eV. Gaussian smearing scheme[8] with a smearing parameter of 0.01 eV was applied in the optimization and frequency calculations, while tetrahedron method with Blöchl corrections[9] adopted in the energies and DOS calculations. The vibrational frequencies were calculated by the finite-difference method with the displacement set to 0.015 Å.

Supplementary Figures

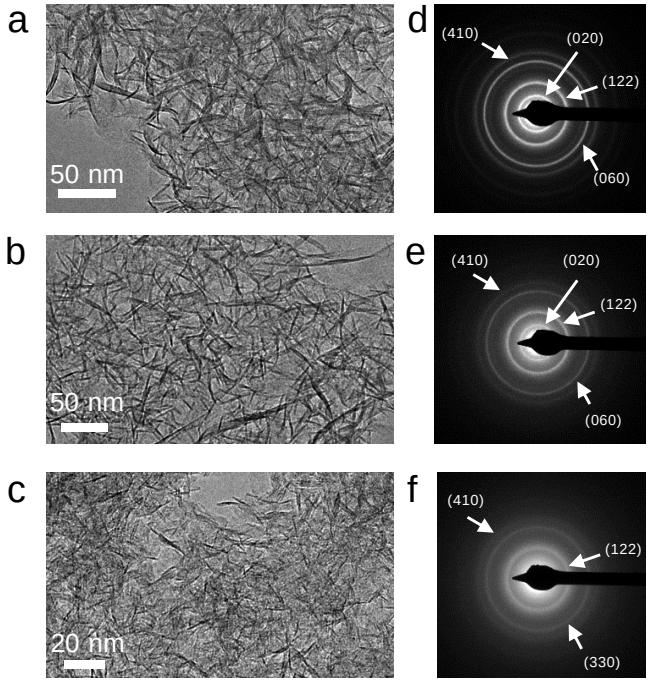

Figure S1. TEM images of (a) CoSHN, (b) FeSHN, (c) NiSHN and SAED patterns of (d) CoSHN, (e) FeSHN, (f) NiSHN.

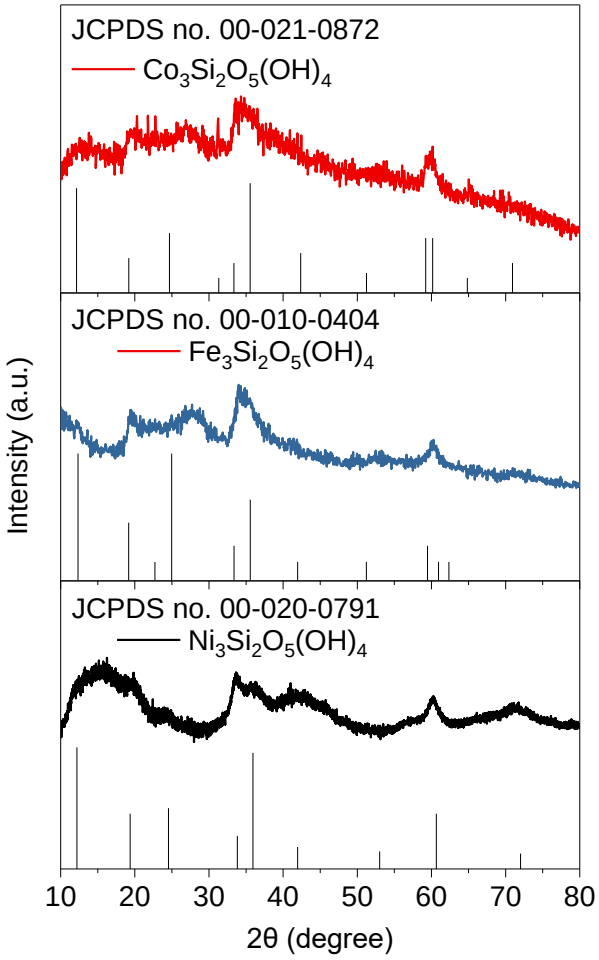

Figure S2. XRD patterns of UMSHN.

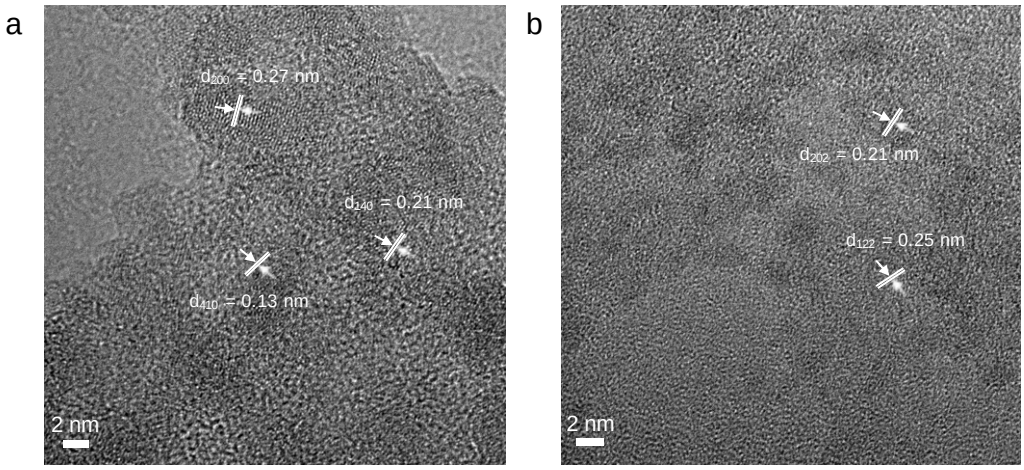

Figure S3. HRTEM images of (a) FeSHN, (b) NiSHN.

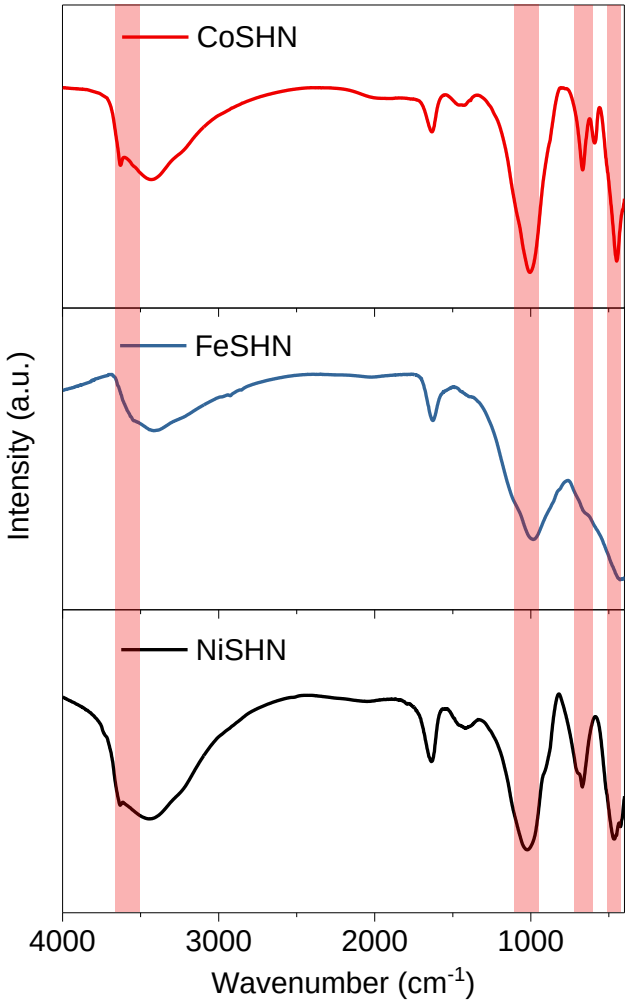

Figure S4. FT-IR spectra of UMSHN.

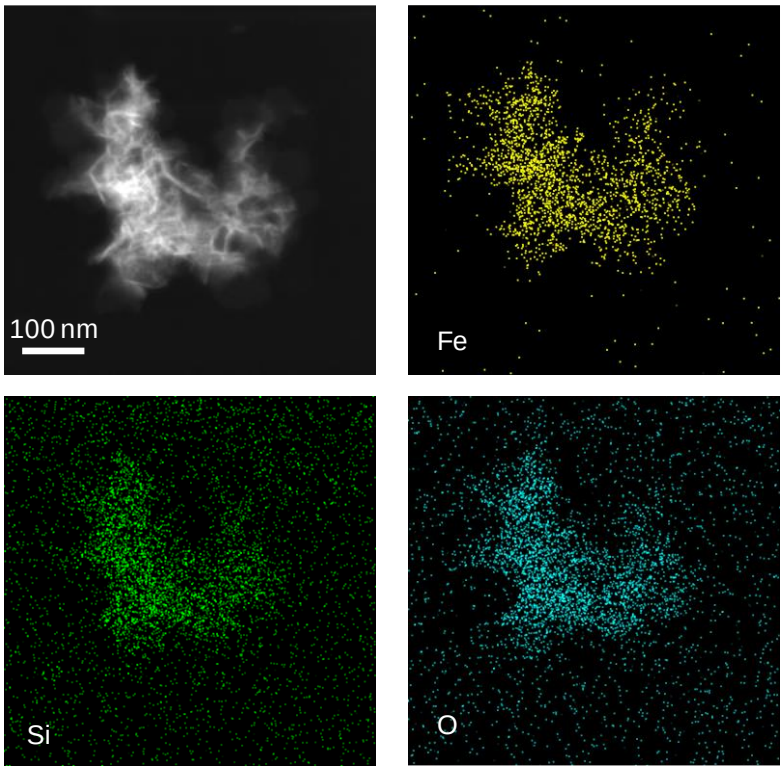

Figure S5. EDX elemental mappings of Fe, Si, O.

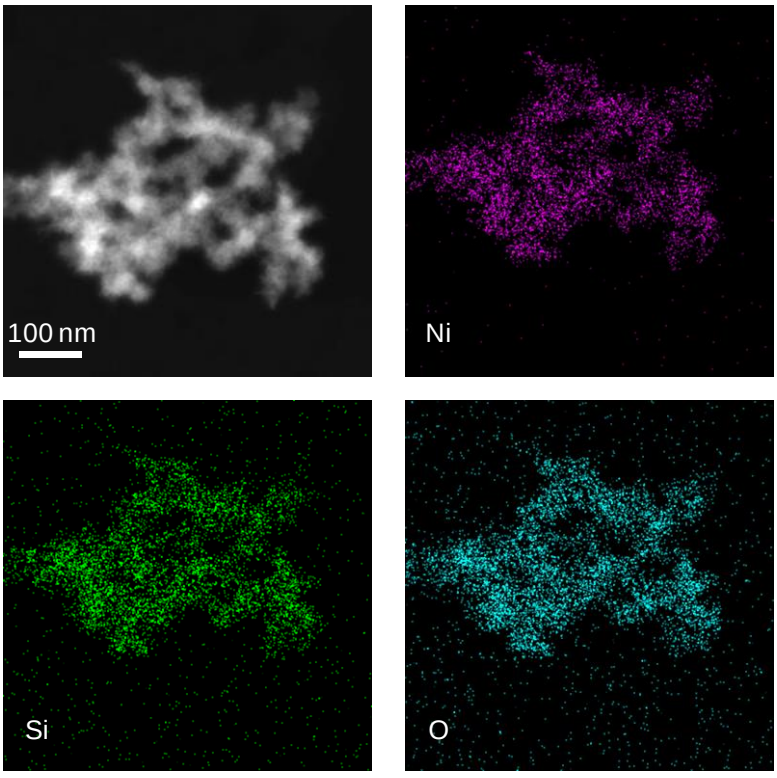

Figure S6. EDX elemental mappings of Ni, Si, O.

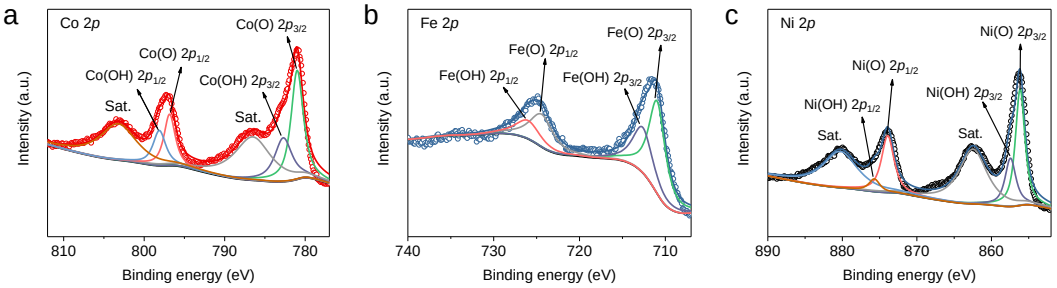

Figure S7. High-resolution XPS spectra of (a) Co 2*p*; (b) Fe 2*p*; and (c) Ni 2*p*.

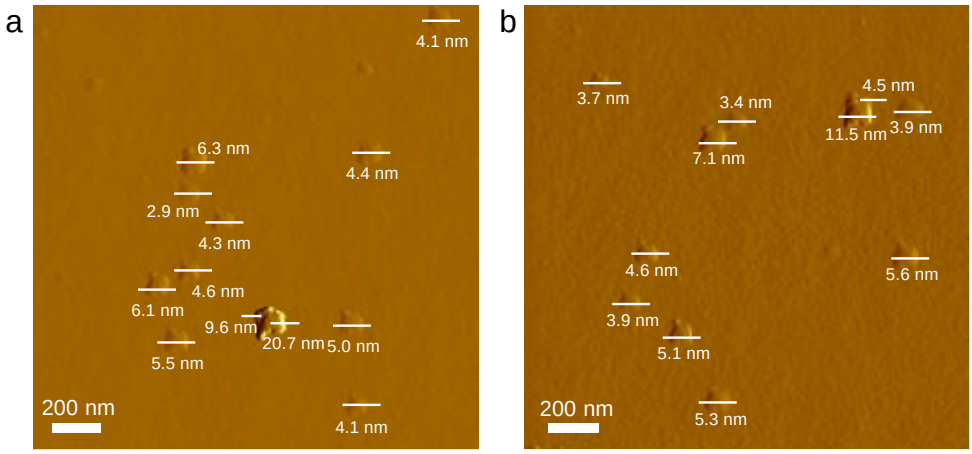

Figure S8. AFM images of (a) FeSHN and (b) NiSHN.

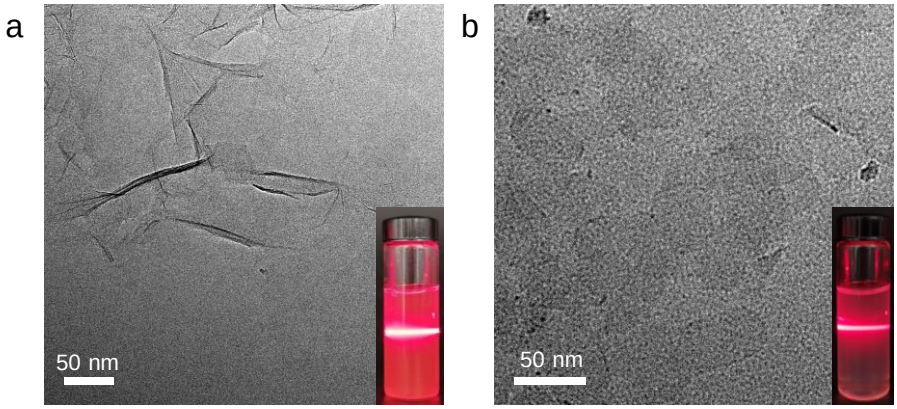

Figure S9. TEM image of (a) FeSHN and (b) NiSHN, the inset shows the Tyndall light scattering of FeSHN and NiSHN in an aqueous solution.

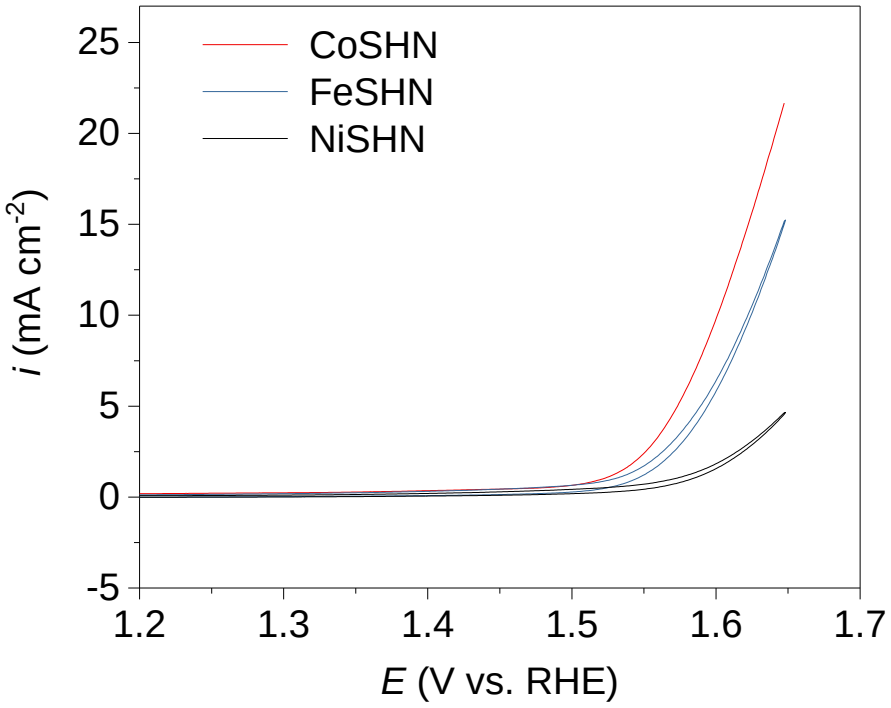

Figure S10. CV curves of MPNS in O_2-saturated 1.0 M KOH without *iR* correction.

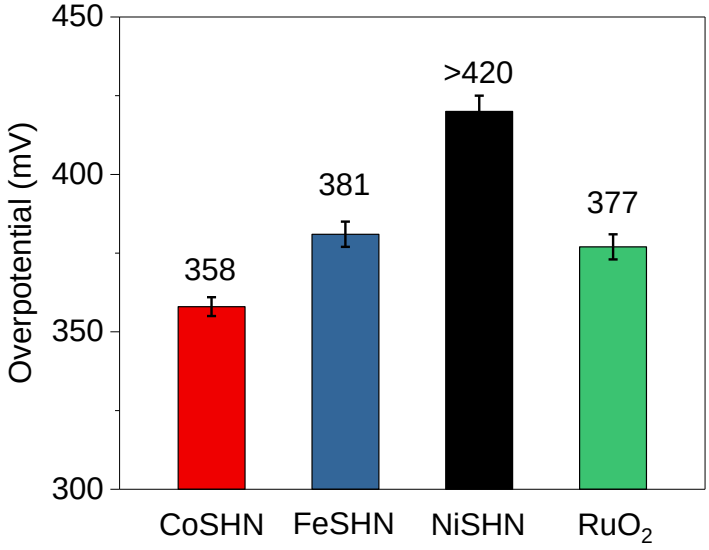

Figure S11. The overpotentials required to reach a current density of 10 mA cm^{-2}.

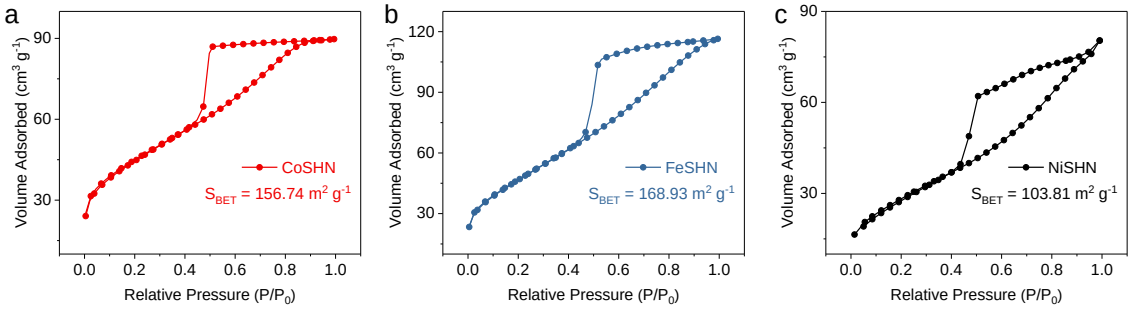

Figure S12. N_2 adsorption-desorption isotherms of (a) CoSHN; (b) FeSHN; and (c) NiSHN.

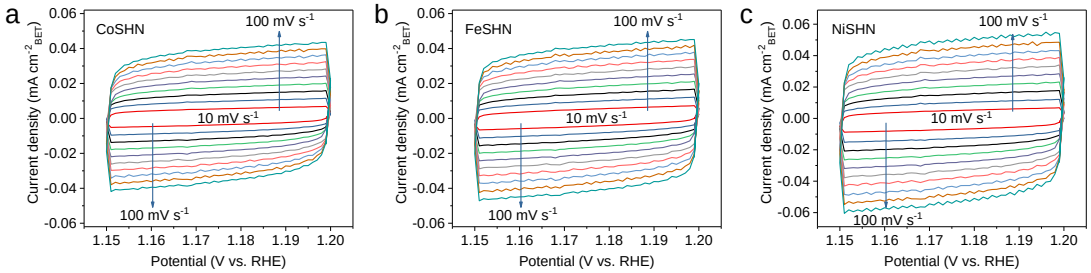

Figure S13. The CV curves with different scan rate under the potential of 1.15 V – 1.20 V of (a) CoSHN, (b) FeSHN and (c) NiSHN.

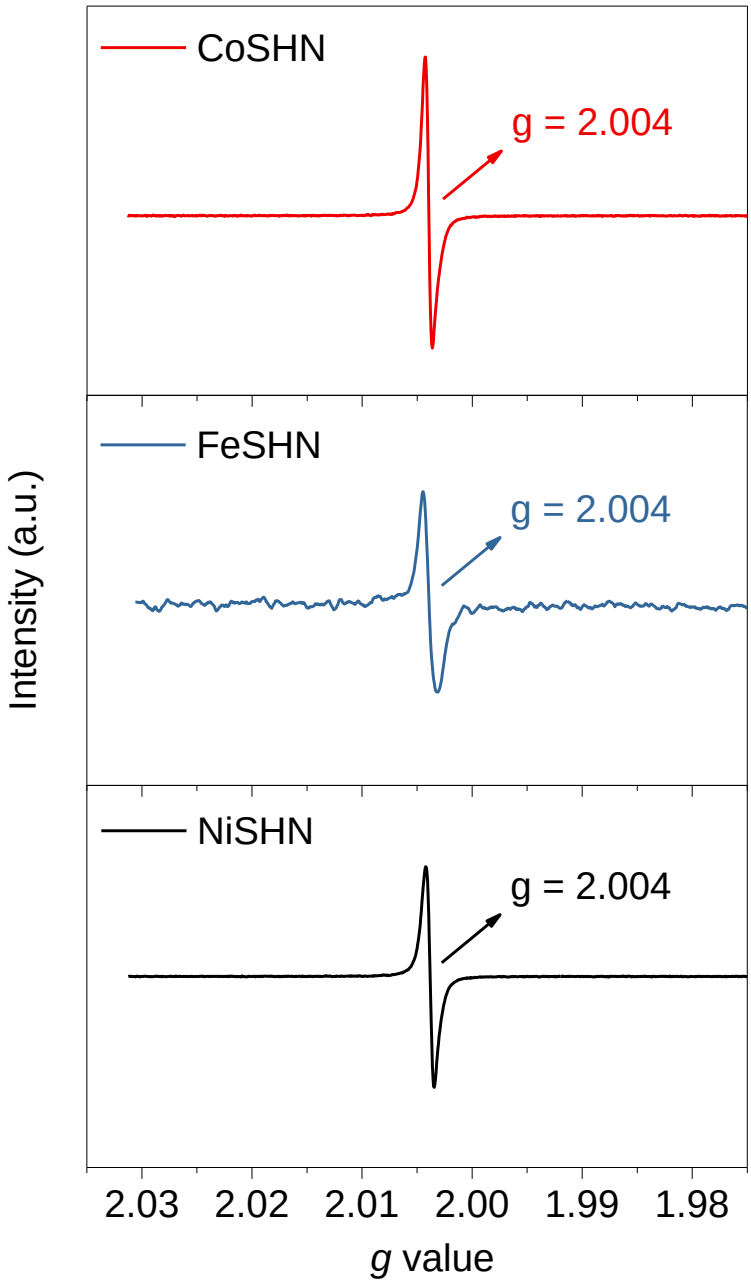

Figure S14. ESR spectra of UMSHN.

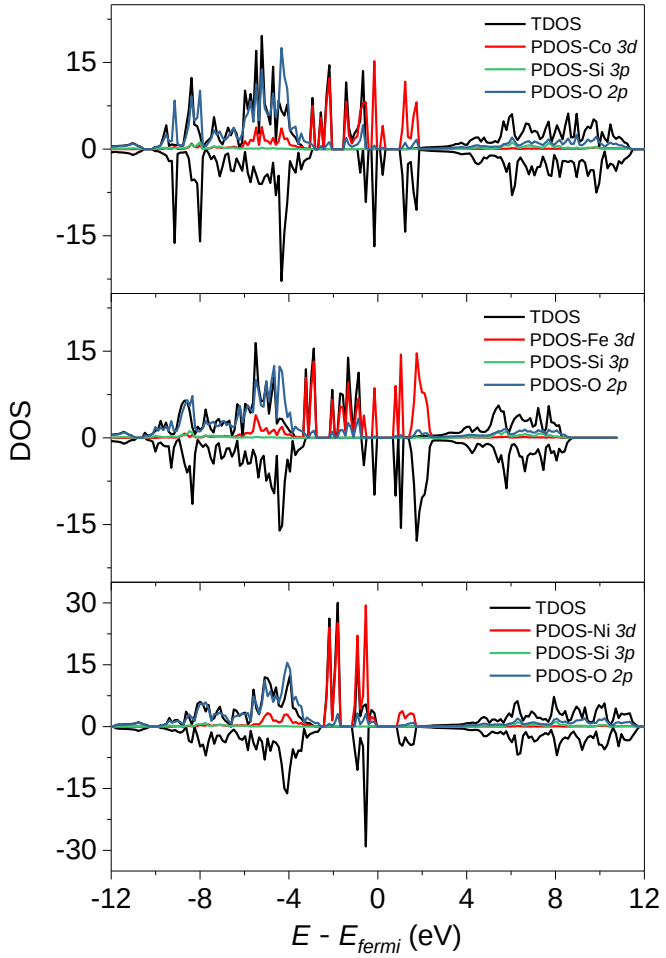

Figure S15. Calculated total density of states (TDOS) and projected density of states (PDOS) reflecting the contributions of different atomic orbitals for UMSHN.

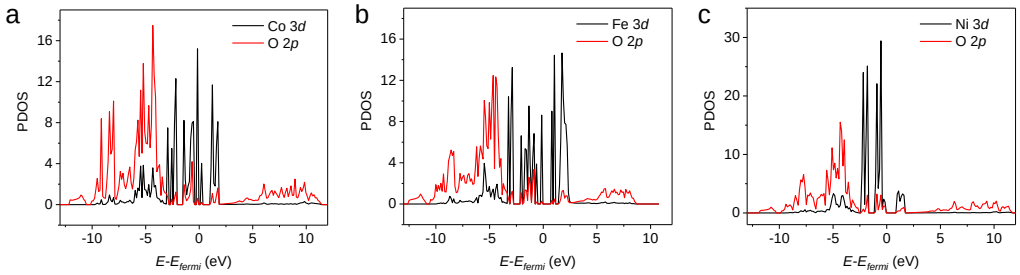

Figure S16. Calculated PDOS for metal 3*d* band and O 2*p* band of (a) CoSHN, (b) FeSHN and (c) NiSHN.

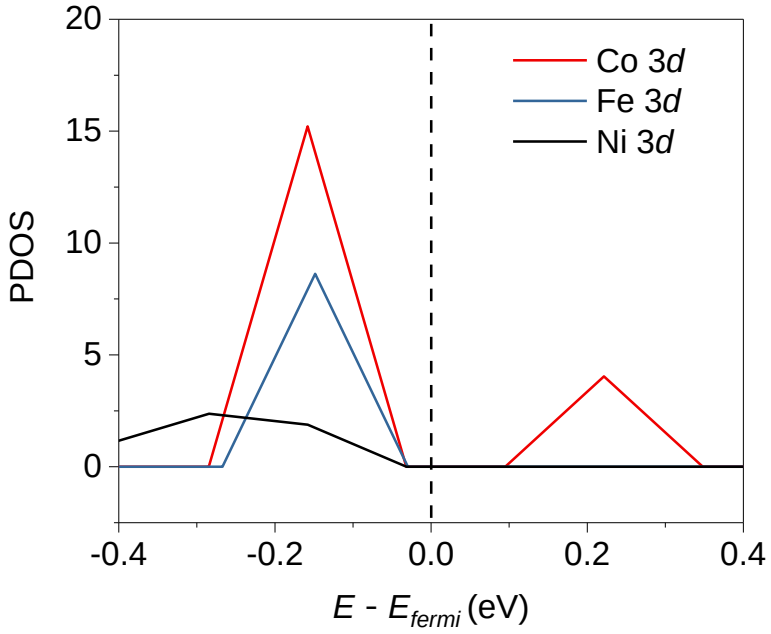

Figure S17. Calculated PDOS for metal 3*d* band.

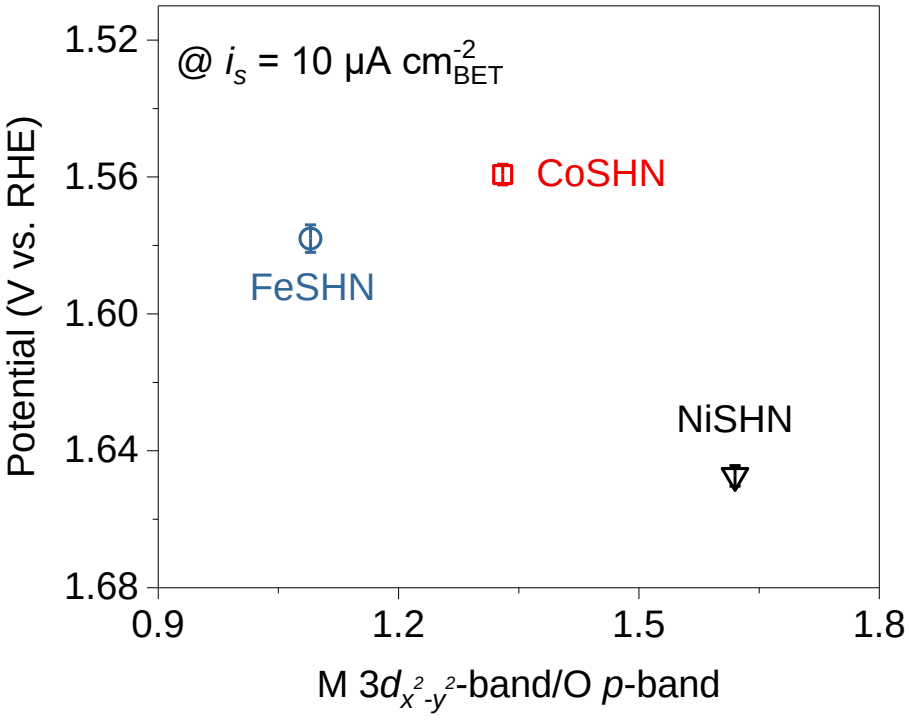

Figure S18. Evolution of the iR-corrected potential at 10 μA cm^{-2} versus the $[3d_{x^2-y^2}]/[2p]$ ratio of the M $3d_{x^2-y^2}$ and O 2*p* contributions to the e_g band of UMSHN.

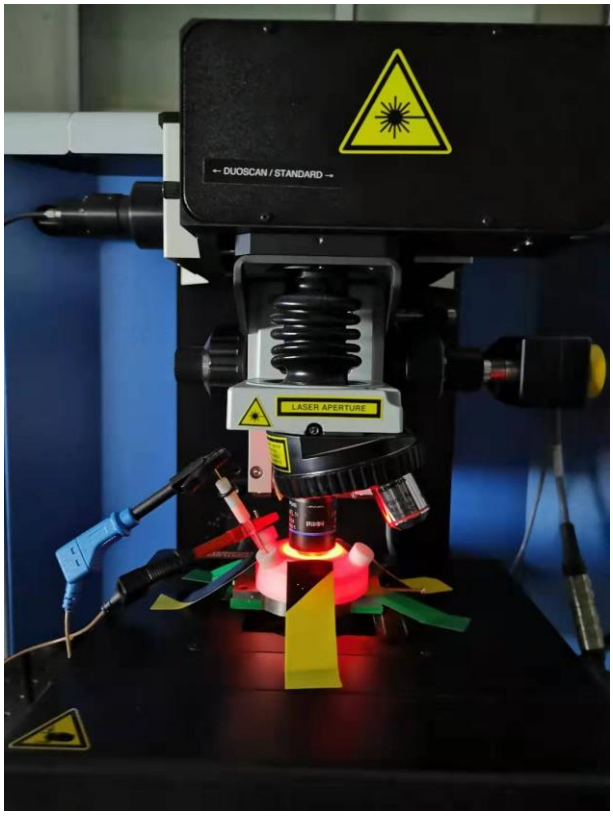

Figure S19. An optical photograph of in-situ electrochemical Raman apparatus with silicate hydroxide electrocatalyst loaded onto GCE as working electrode, together with a Pt wire counter electrode and an Ag/AgCl reference electrode.

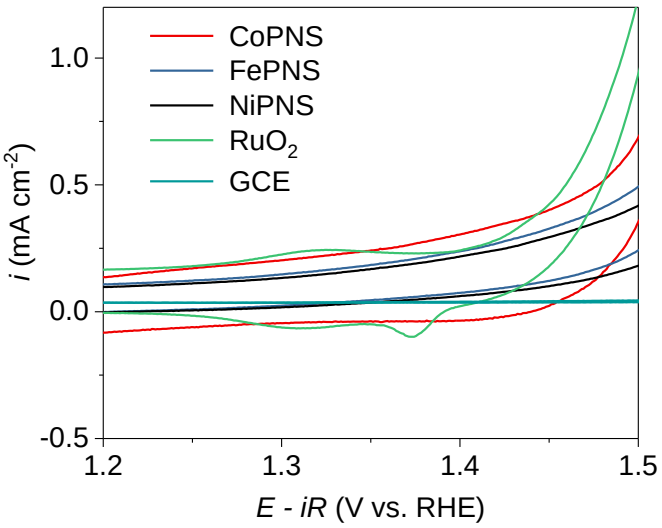

Figure S20. CV curves of UMSHN, GCE and commercial RuO_2 in O_2-saturated 1.0 M KOH.

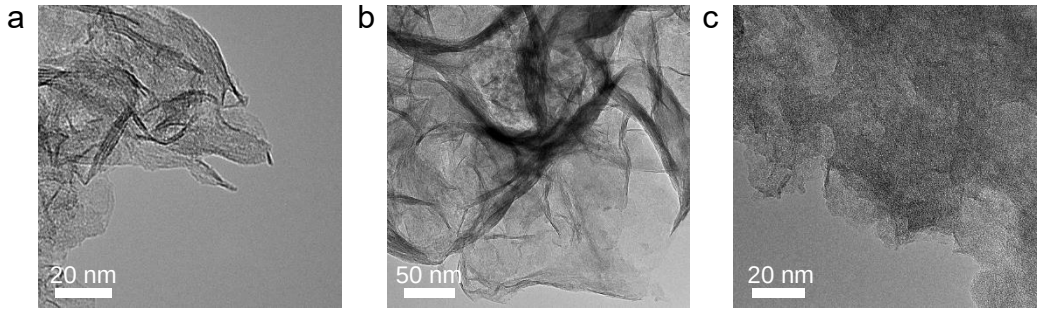

Figure S21. TEM images of CoSHN (a), FeSHN (b) and NiSHN (c) after OER electrocatalysis.

Table S1 Comparison of OER performance of UMSHN with single metal oxides electrocatalysts recently reported.

Catalysts	Electrolytes	Substrate	j (mA cm^{-2})	η (mV)	Tafel slope (mV dec^{-1})	Reference
CoSHN	1.0 M KOH	GCE[a]	10	358	58.6	This work
FeSHN	1.0 M KOH	GCE	10	381	66.5	This work
NiSHN	1.0 M KOH	GCE	10	>420	74.5	This work
CoOOH PNSAs	1.0 M KOH	CFC[b]	10	331	56.4	10
ACP	1.0 M KOH	GCE	10	364	60	11
Co-UNMs	1.0 M KOH	GCE	10	307	76	12
LCO	0.1 M KOH	GCE	10	370	69	13
$Ni(OH)_2$	1.0 M KOH	GCE	10	338	47	14
MnO_2	0.1 M KOH	GCE	10	500	93	15
MnO_2/CFP	1.0 M KOH	CFP[c]	10	467	111.7	16
CoO_x-ZIF	1.0 M KOH	GCE	10	318	70.3	17
2DNWS	1.0 M KOH	GCE	10	358.2	54.4	18

[a]GCE = glass carbon electrode, [b]CFC = carbon fiber cloth, [c]CFP = carbon fiber paper.

Reference

1. G. Kresse and J. Furthmüller, *Computational materials science*, 1996, **6**, 15-50.
2. G. Kresse and J. Furthmüller, *Physical review B*, 1996, **54**, 11169.
3. J. P. Perdew, K. Burke and M. Ernzerhof, *Phys. Rev. Lett.*, 1996, **77**, 3865.
4. J. P. Perdew, *Physical Review B*, 1986, **33**, 8822.
5. G. Kresse and D. Joubert, *Physical Review B*, 1999, **59**, 1758.

6. P. E. Blöchl, *Physical review B*, 1994, **50**, 17953.
7. H. J. Monkhorst and J. D. Pack, *Physical review B*, 1976, **13**, 5188.
8. M. Methfessel and A. Paxton, *Physical Review B*, 1989, **40**, 3616.
9. P. E. Blöchl, O. Jepsen and O. K. Andersen, *Physical Review B*, 1994, **49**, 16223.
10. S. H. Ye, Z. X. Shi, J. X. Feng, Y. X. Tong and G. R. Li, *Angew. Chem., Int. Ed.*, 2018, **57**, 2672-2676.
11. J. S. Kim, I. Park, E. S. Jeong, K. Jin, W. M. Seong, G. Yoon, H. Kim, B. Kim, K. T. Nam and K. Kang, *Adv. Mater.*, 2017, **29**, 1606893.
12. Y. Li, F.-M. Li, X.-Y. Meng, S.-N. Li, J.-H. Zeng and Y. Chen, *ACS Catal.*, 2018, **8**, 1913-1920.
13. S. Zhou, X. Miao, X. Zhao, C. Ma, Y. Qiu, Z. Hu, J. Zhao, L. Shi and J. Zeng, *Nat. Commun.*, 2016, **7**, 11510.
14. G. Liu, P. Li, G. Zhao, X. Wang, J. Kong, H. Liu, H. Zhang, K. Chang, X. Meng, T. Kako and J. Ye, *J. Am. Chem. Soc.*, 2016, **138**, 9128-9136.
15. M. Fekete, R. K. Hocking, S. L. Y. Chang, C. Italiano, A. F. Patti, F. Arena and L. Spiccia, *Energy Environ. Sci.*, 2013, **6**.
16. Z. Ye, T. Li, G. Ma, Y. Dong and X. Zhou, *Adv. Funct. Mater.*, 2017, **27**.
17. S. Dou, C.-L. Dong, Z. Hu, Y.-C. Huang, J.-l. Chen, L. Tao, D. Yan, D. Chen, S. Shen, S. Chou and S. Wang, *Adv. Funct. Mater.*, 2017, **27**.
18. Y. Dou, L. Zhang, J. Xu, C.-T. He, X. Xu, Z. Sun, T. Liao, B. Nagy, P. Liu and S. X. Dou, *ACS Nano*, 2018, **12**, 1878-1886.